Polymer Degradation and Stability 245 (2026) 111873

Contents lists available at ScienceDirect

Polymer Degradation and Stability

journal homepage: www.journals.elsevier.com/polymer-degradation-and-stability

# Bioplastic films from *Sargassum oligocystum* and *Eucheuma spinosum* seaweeds: Preparation, thermal degradation, and kinetics analysis

Alulutho Ngonyamana [a,b], Bothwell Nyoni [a,c], Jabulani I. Mnyango [a,b,*], Invine T. Kandirai [d], Shanganyane P. Hlangothi [a,b], Sudhakar Muniyasamy [a,e,*]

[a] Department of Chemistry, Nelson Mandela University, P.O. Box 77000, Gqeberha 6031, South Africa
[b] Centre for Rubber Science and Technology, Nelson Mandela University, P.O. Box 77000, Gqeberha 6031, South Africa
[c] Department of Applied Chemistry, National University of Science and Technology, P.O. Box AC 936, Ascot, Bulawayo, Zimbabwe
[d] Department of Chemical Sciences, Midlands State University, P. Bag 9055, Gweru, Zimbabwe
[e] Centre for Nanostructures and Advanced Materials, Council for Scientific and Industrial Research, Pretoria 0001, South Africa

ARTICLE INFO

*Keywords:*
Bioplastic films
Seaweed-derived biopolymers
*Sargassum* spp.
*Eucheuma* spp.
Thermal degradation
Kinetic modeling

ABSTRACT

In the framework of a circular economy, bioplastics derived from renewable natural resources are gaining attention as sustainable alternatives to conventional plastics. This study reports the synthesis of bioplastic films from brown seaweed (*Sargassum oligocystum*) and red seaweed (*Eucheuma spinosum*) *via* alginate extraction, followed by structural and thermal characterization. Fourier-transform infrared spectroscopy, X-ray diffraction, thermogravimetric analysis, and differential scanning calorimetry results confirmed that *Sargassum oligocystum*-based bioplastic exhibited properties comparable to the commercial sodium alginate-derived bioplastic. Additionally, thermogravimetric analysis results revealed that *Sargassum oligocystum* decomposed in a single step near 220 °C, whereas *Eucheuma spinosum* degraded in two steps at ≈ 280 °C and 330 °C. The corresponding bioplastic films showed decomposition at ≈ 225 °C (*Sargassum oligocystum*) and 250 °C (*Eucheuma spinosum*). Kinetic studies indicated nucleation-controlled thermal degradation, with activation energies of 20.0 to 26.8 kJ/mol for *Eucheuma spinosum* and 43.8 to 49.5 kJ/mol for *Sargassum oligocystum* bioplastics. These findings demonstrate the potential of seaweed-derived bioplastics as renewable, thermally stable materials and provide insights into their degradation mechanisms for future material optimization and practical applications.

## 1. Introduction

The escalating challenges of plastic pollution and the imminent depletion of fossil resources have created an urgent demand for sustainable alternatives to petroleum-based plastics. Bioplastics derived from renewable sources such as plants and algae are emerging as promising substitutes, with potential applications in packaging, biomedical devices, and other sectors [1,2]. Within the framework of a circular economy, these materials are particularly attractive as they can be produced from renewable or recycled feedstocks, thereby reducing reliance on finite fossil resources and mitigating the environmental impacts of persistent plastic waste, including landfill accumulation, marine pollution, and extended degradation times [3,4].

Seaweeds have recently gained attention as a sustainable feedstock for bioplastic production due to their abundance, biodegradability, and rich polysaccharide content [5,6]. Unlike terrestrial biomass, seaweeds do not require arable land, freshwater, or pesticides, which makes them especially advantageous from an environmental perspective [7–9]. Among various species, *Sargassum oligocystum* (*S. oligocystum*, brown seaweed) and *Eucheuma spinosum* (*E. spinosum*, red seaweed) have been recognized as potential candidates for bioplastic synthesis, as their polysaccharides can be extracted to produce biodegradable films [6]. Conventional plastics such as polyethylene (PE), polypropylene (PP), and polyethylene terephthalate (PET), in contrast, are typically derived from fossil fuels and are non-biodegradable, contributing to severe ecological risks [10–13]. Bioplastics from seaweeds, owing to their biodegradability and reduced ecological footprint, are increasingly viewed as promising substitutes [5,6].

Despite this potential, there remains a significant knowledge gap regarding the thermal degradation behavior and decomposition kinetics of seaweed-derived bioplastics. Thermal stability is a critical property, as it affects material performance during processing and determines its

* Corresponding authors.
*E-mail addresses:* s216281547@mandela.ac.za (J.I. Mnyango), smuniyasamy@csir.co.za (S. Muniyasamy).

https://doi.org/10.1016/j.polymdegradstab.2025.111873
Received 2 October 2025; Received in revised form 4 December 2025; Accepted 18 December 2025
Available online 18 December 2025

applicability in higher-temperature environments. While previous studies have explored general properties of seaweed-based bioplastics, comprehensive investigations into their thermal degradation pathways and kinetic mechanisms remain limited, particularly for *S. oligocystum* and *E. spinosum* [14–18]. Some preliminary studies have reported partial thermal or mechanical data for *S. oligocystum* [19,20] and *E. spinosum* [21,22], but these are fragmented and do not provide a full comparative analysis of their degradation behaviors or derived bioplastic films. Such understanding is essential for optimizing processing conditions, improving material performance, and facilitating commercial adoption.

Moreover, thermal degradation characteristics can vary considerably across seaweed species due to differences in biochemical composition and extraction methods. Some seaweeds undergo single-step decomposition, whereas others degrade through multiple stages [23–25]. Kinetic studies further provide insights into activation energies ($E_a$), reaction mechanisms, and degradation rates, all of which are vital for industrial-scale development [26,27]. However, comparative data on the degradation behaviors of *S. oligocystum* and *E. spinosum*, as well as their corresponding bioplastic films, remain scarce. This highlights the novelty of the present study, which systematically compares the thermal degradation and kinetics of these two seaweed species and their bioplastic films under controlled conditions.

This work aims to address this research gap by synthesizing bioplastic films from *S. oligocystum* and *E. spinosum*, evaluating their thermal degradation behavior using TGA, and analyzing their degradation kinetics. By comparing the thermal stability of raw seaweeds with their derived bioplastic films, this work provides new insights into their degradation mechanisms and stability profiles. Overall, the study contributes to the growing body of knowledge on seaweed-derived bioplastics and supports their potential as renewable, sustainable alternatives to conventional plastics, aligning with broader efforts toward a circular economy.

## 2. Experimental

### 2.1. Materials and preparation of dried and ground seaweeds

The *S. oligocystum* samples were obtained from Mwani Seaweed Centre, Zanzibar, Tanzania, while *E. spinosum* was obtained from Kelpy Biotechnology Research, Jervis Bay, NSW, Australia. The raw seaweeds were manually inspected to remove visible impurities such as stones and sand, then washed three times with distilled water to reduce residual salt. Following washing, the samples were freeze-dried until constant weight (≈ three days) and subsequently air-dried for five days. The dried seaweeds were ground into fine powder using a household grinder and sieved through a 60-mesh sieve (250 $\mu$m) to ensure uniformity. Moreover, all chemicals used were of analytical grade and purchased from Sigma-Aldrich Merck (Merck KGaA, Darmstadt, Germany): ethanol (99 %, ACS reagent grade) and acetone (≥ 99 %, ACS reagent grade), glycerol (≥ 99 %, ACS reagent grade), concentrated hydrochloric acid (HCl, 37 %, ACS reagent grade), anhydrous calcium chloride ($CaCl_2$, ≥ 99 %, ACS reagent grade), and sodium carbonate ($Na_2CO_3$, ≥ 99 %, ACS reagent grade). They were used in the preparation, extraction, and processing of the seaweed samples, as well as in the synthesis of bioplastic films.

### 2.2. Alginate extraction and film synthesis

Solutions of $CaCl_2$ and $Na_2CO_3$ were prepared separately. Anhydrous $CaCl_2$ (6 g; 0.216 M) was dissolved in 250 mL of distilled water, and $Na_2CO_3$ (19 g; 0.716 M) was dissolved in the same volume of distilled water. Because both salts are hygroscopic, they were weighed in a sealable container to prevent moisture uptake. The preparation method followed the procedure described by Bojorges *et al.* [28]. For alginate extraction, 20 g of dried and ground seaweed sample was placed in a 500 mL Erlenmeyer flask containing 250 mL of a 2 % (w/v; 0.18 M) $CaCl_2$ solution. The mixture was stirred at 150 rpm for 24 h. The samples were then filtered and washed three times with an excess of distilled water. Each sample was subsequently immersed in 20 mL of 0.2 M HCl for 1 h, followed by filtration and three washes with 300 mL of distilled water. The samples were then transferred to 500 mL Erlenmeyer flasks containing 250 mL of a 2 % (w/v; 0.19 M) $Na_2CO_3$ solution and incubated overnight at ambient temperature. After incubation, the mixtures were centrifuged at 100 rpm for 2 min to separate the solid residues from the solution. The supernatant was collected, washed three times with a 1:1 ethanol–distilled water solution, and air-dried for 2 h. Finally, the extracts were oven-dried in an air-circulating oven at 50 °C for 24 h to ensure complete drying. These extraction steps ($CaCl_2$ pre-treatment, acidic washing, and $Na_2CO_3$ solubilisation) also facilitate the removal of mineral matter from the alginate matrix. The subsequent triple washing with distilled water and the ethanol–water purification step further reduced inorganic residues, ensuring that the final extracts contained minimal mineral contaminants. This purification was essential to avoid interference with thermal behaviour and degradation kinetics, as residual minerals may act as inorganic fillers or catalytic sites during decomposition.

Films were synthesized separately from the *S. oligocystum* and *E. spinosum* extracts. Each extract (10 g; 1:15 w/v) was transferred to a 250 mL Erlenmeyer flask containing 150 mL of distilled water and heated to 80 °C with continuous stirring (150 rpm) for 30 min to ensure complete dissolution. Upon reaching 80 °C, glycerol (20 % w/w of the extract) was added as a plasticizer, and stirring continued until gelatinization occurred. The solutions were further heated to 90 °C for 3 min, then poured into petri dishes and dried in an air-circulating oven at 50 °C for five days to ensure complete moisture removal and uniform film formation. The resultant bioplastic films were carefully peeled from the petri dishes and stored for subsequent analyses. All film synthesis and extraction procedures were performed in triplicate to ensure reproducibility, and representative mean values were reported for subsequent analyses. A control experiment was conducted using commercial-grade sodium alginate, following the same procedure. The samples used in this study were labelled as RSW, BSW, RSWE, BSWE, SA, RSWBP, BSWBP, and CEBP, corresponding to red seaweed (dried and ground raw material), brown seaweed (dried and ground raw material), red seaweed extract, brown seaweed extract, sodium alginate, red seaweed bioplastic, brown seaweed bioplastic, and control experiment bioplastic, respectively.

### 2.3. Characterization

#### 2.3.1. Determination of organic and mineral content

Proximate analysis was performed using a muffle furnace following the procedures outlined in the standard methods ASTM E871 [29] and ASTM E872 [30]. Each proximate analysis parameter (moisture, volatile matter, fixed carbon, and ash content) was determined in triplicate ($n = 3$) to ensure analytical reproducibility, and the reported values represent the mean of replicate measurements. The analysis was used to determine the fixed carbon, volatile matter, and ash of the raw materials. Ash content represents the total mineral content. High ash may indicate excessive sand, salt, or inorganic impurities, which can lower alginate yield or quality. The ash content of the raw seaweeds was also used to estimate the mineral load prior to extraction, enabling assessment of the extent of mineral removal after alginate purification. Fixed carbon and volatiles aid in estimating the proportion of organic matter available for conversion into alginate and other products.

#### 2.3.2. Identification of functional groups

The Fourier-transform infrared (FT-IR) spectroscopy was conducted using an Alpha Bruker FT-IR spectrometer to assess the functional groups present in the samples. FT-IR spectra of the samples were recorded using Opus software over a wavenumber range of 4000–400 $cm^{-1}$, with 32 scans per sample at a resolution of 4 $cm^{-1}$. Background

measurements were used to standardize each spectrum.

#### 2.3.3. Crystallinity and particle size analysis

X-ray diffraction (XRD) analysis was performed using a powder XRD (PXRD) instrument (Bruker 2D 2nd Gen diffractometer) using Cu Kα-radiation (λ = 1.5406 Å) at ambient temperature. The samples were placed onto a zero-background sample holder and scanned over a 2θ range of 4 to 90° with a step of 0.300 increments. X-rays were generated with a current flow of 10 mA and a voltage of 30 kV. The Scherrer equation (*Eq. (1)*) was used to estimate the crystalline size of the seaweed bioplastics:

$$D = \frac{K\lambda}{\beta\cos[\theta]} \tag{1}$$

The average particle size (nm) of the bioplastic samples is represented by $D$, $\lambda$ is the X-ray wavelength (nm), $K$ is a constant, $\theta$ is the Bragg angle in radians, and $\beta$ is the excess line broadening expressed in radians.

#### 2.3.4. Thermal stability and degradation behavior

The thermal behavior of the samples was studied using a Perkin Elmer (STA 6000) simultaneous thermal analyzer instrument. The analysis was performed on samples weighing between ≈ 4 and 5 mg placed in a thermobalance pan of the instrument, where inert conditions were achieved by maintaining a constant flow of $N_2$ at 20 mL/min. The heating rates used for the analyses were 10, 15, and 20 °C/min, and the temperature range was between ≈ 40 °C and 600 °C. Mass-loss (TG) and heat flow (DSC) data were extracted, analysed, and presented using the Start Pyris and MS Excel software packages. Because inorganic residues can influence thermal degradation by promoting catalytic cracking or altering char formation, the low mineral content achieved after extraction ensured that the thermal degradation profiles reflected primarily the polymeric behaviour of the bioplastics rather than mineral-catalysed processes.

### 2.4. Kinetic analysis of thermal degradation

Thermal decomposition of most biomass materials is a complex process; as such, care is generally taken in the selection of the decomposition kinetics analysis methods. It is advisable to explore both model-fitting and model-free methods. The Kissinger and Coats-Redfern (CR) methods are the most popular model-fitting methods, whereas various model-free methods have been used by researchers in the field. In this work, the CR method and two model-free methods, *i.e.,* the Kissinger-Akahira-Sunose (KAS) and Ozawa-Flynn-Wall (OFW), were used to analyse the mass-loss data generated from the TGA experiments. Using model-fitting and model-free methods will present an opportunity to compare the results generated. This will help improve the understanding of the thermal decomposition behaviour and kinetics of the process because model-free methods give reliable kinetic parameters, while model-fitting provides mechanistic insight.

The Kissinger method estimates a single apparent $E_a$ for the reaction based on the temperature at which the maximum rate of decomposition occurs ($T_m$). It is assumed that the reaction is single-step and follows a simple first-order kinetic model. The peak temperature corresponds to the maximum reaction rate and represents the reaction as a whole. The equation (*Eq. (2)*) derived from the Arrhenius equation is as follows [31]:

$$\mathrm{In}\left(\frac{\beta}{T_m^2}\right) = \mathrm{In}\left(\frac{AR}{E_a}\right) - \frac{E_a}{RT_m} \tag{2}$$

$A$ is the pre-exponent factor in the Arrhenius equation, $R$ is the universal gas constant (0.0083 kJ/mol.K), $\beta$ is the heating rate (K/min), and $E_a$ is the activation energy (kJ/mol). A straight line fit of $\mathrm{In}\left(\frac{\beta}{T_m^2}\right)$ *vs.* $\frac{1}{T_m}$ will give a slope equivalent to $-\frac{E_a}{R}$.

For the CR method, model fitting can be done for several available kinetic model functions, *g(X)*, following *Eq. (3)* and *Eq. (4)*, the derivation of these equations is found in the literature [31,32].

$$g(X) = \left(\frac{ART^2}{E_a\beta}\right)exp\left(\frac{-E_a}{RT}\right) \tag{3}$$

$$\mathrm{In}\left[\frac{g(X)}{T^2}\right] = \mathrm{In}\frac{AR}{\beta E_a}\left[1 - \frac{2RT}{E_a}\right] - \frac{E_a}{RT} \tag{4}$$

In these equations, $T$ is the temperature (K) at a conversion ratio of $X$, and $n$ is the order of reaction. For the pyrolysis temperature range used in this study, the first term on the right-hand side of *Eq. (4)* can be regarded as a constant because $\frac{2RT}{E_a}$ is very small [33]. *Eq. (4)* can be plotted as a straight line fit with $\mathrm{In}\left[\frac{g(X)}{T^2}\right]$ taking the y-values and $\frac{1}{T}$ taking the *x*-values. The slope and y-intercept of the straight line are used to evaluate the $E_a$ and the pre-exponential factor.

The KAS and OFW methods depend on a series of TGA mass-loss data that is obtained from at least three different heating rates. The kinetic parameters are determined by recording the reaction exothermic peak temperature at each heating rate. Model-free methods do not require a specific kinetic model (*e.g.,* reaction order, rate equation) to be assumed in advance. This makes them particularly useful when the underlying reaction mechanism is unknown or complex. These methods can help identify whether a process involves multiple reaction steps or mechanisms. The simplified linear equations for the KAS and OFW methods are given in *Eqs. (6)* and *(7)* [32,34,35].

$$\mathrm{In}\left(\frac{\beta}{T^2}\right) = \mathrm{In}\left(\frac{AR}{E_a}\right) - \frac{E_a}{RT} \tag{6}$$

$$\log(\beta) = \log\left(A\frac{E_A}{Rg(X)}\right) - 2.315 - 0.4567\frac{E_a}{RT} \tag{7}$$

whereby *f(X)* is a function of the conversion and *g(X)* is the integral form of *f(X)*. Similarly, *Eqs. (6)* and *(7)* can be plotted as a straight line of $\mathrm{In}\left(\frac{\beta}{T^2}\right)$ and $\mathrm{In}(\beta)$ respectively, *vs.* $\frac{1}{T}$. The slope and y-intercept of the lines are used to evaluate the $E_a$ and the pre-exponential factor.

## 3. Results and discussion

### 3.1. Proximate analysis of seaweed

Knowing proximate composition provides insight into the availability of film-forming polysaccharides and the balance of other constituents that affect processing, mechanical strength, biodegradability, and overall performance of seaweed-based bioplastics. Table 1 presents the proximate composition of the two seaweed samples analyzed. Since the analyses were performed in triplicate and the variation among replicates was within 5 %, only the mean values are reported in Table 1 for clarity. Although the samples were obtained from different locations, their compositions are comparable and fall within the typical ranges reported for seaweeds in previous studies. For instance, the *S. oligocystum* and *E. spinosum* composition results are in agreement with the works of Chowdhury *et al.* [36] and Premarathna *et al.* [37], who reported ash composition of *Sargassum* spp. to be in the range 8 to 20 %.

**Table 1**
Proximate analysis of the seaweeds (mean values from triplicate measurements, $n = 3$).

| Seaweed | Moisture ( %) | Volatiles ( %) | Fixed carbon ( %) | Ash ( %) |
|---|---|---|---|---|
| *S. oligocystum* | 13 | 33 | 34.6 | 19.4 |
| *E. spinosum* | 17 | 43 | 21.8 | 18.2 |

The high fixed carbon and volatile matter content of the two seaweeds indicates their richness in polysaccharides (*e.g.,* alginate, carrageenan, agar, and cellulose), which serve as the primary film-forming agents in bioplastics, suggesting that these seaweeds have significant potential as raw materials for bioplastic synthesis. Even so, further processing procedures like drying and mineral removal are necessary to optimize their use in bioplastic synthesis due to their significantly high ash and moisture content [38]. The ash content is a result of their cell wall polysaccharides and protein containing anionic carboxyl, sulphate, and phosphate groups [36].

### 3.2. Crystallinity and structural

XRD analysis was conducted to examine the crystallinity and particle sizes of the bioplastic films, CEBP, RSWBP, and BSWBP. As illustrated in Fig. 1, the diffraction patterns of all samples exhibit features typical of bioplastics, marked by peaks corresponding to amorphous regions. A prominent peak was observed at 19.39° for both CEBP and BSWBP, which shifted slightly to 21.81° in the case of RSWBP. Additionally, all three films displayed a broad peak near 62.29°, showing their amorphous nature. Notably, RSWBP exhibited distinct sharp peaks at 28.68° and 40.85°, indicative of a higher degree of crystallinity, which suggests lower biodegradability [39,40]. Among the samples, BSWBP showed a more amorphous structure compared to CEBP and RSWBP, implying it may decompose more readily [41]. The crystalline size of the bioplastics CEBP, RSWBP, and BSWBP was found to be 1.419, 0.9709, and 1.5532, respectively. The prepared BP films were cast in circular molds of *ca.* 5 cm diameter, with an average thickness of *ca.* 0.2 mm, typical for lab-scale seaweed-derived bioplastics. These dimensions allowed for consistent handling and characterization across all analyses.

### 3.3. Synthesis pathway and thermal-structural properties

Fig. 2 shows the TG, DTG, and FT-IR results of the seaweed raw materials, the corresponding bioplastic films, and the commercial sodium alginate-derived extract, highlighting their thermal degradation behavior and compositional features. The TG and DTG curves for the seaweed raw materials revealed that, apart from inherent moisture, BSW has one major constituent that decomposes at ≈ 275 °C, whilst RSW is composed of two major constituents that decompose at 275 and 350 °C. These constituents are carbohydrates and proteins, which are known to be the major building blocks for seaweed and other biomass materials, and they decompose in the temperature range of 160 to 300 °C and 320 to 450 °C, respectively [42]. The thermal degradation characteristic parameters of seaweeds, extracts, and bioplastics are given in Table 2. It can be seen that the thermal decomposition characteristic parameters, *i.e.*, degradation onset temperature ($T_o$), peak degradation temperature ($T_p$), final degradation temperature ($T_f$) and peak reactivity ($R_p$) are different for the raw materials (BSW and RSW) and their respective extracts (BSWE and RSWE). From the DTG curves, it can be inferred that BSW (Fig. 2d) is a more suitable raw material for bioplastic synthesis, owing to its higher reactivity, which is an indicator of higher carbohydrate and polysaccharide content. These polysaccharides, which may include alginate, carrageenan, agar, or cellulose, depending on the seaweed species, function as the principal film-forming agents in bioplastic production. Furthermore, the shape of the DTG curves of BSWE and RSWE, when overlaid with that of commercial-grade alginate (SA) (Fig. 2e), confirms that the extraction procedure employed successfully isolated alginate from the seaweed samples. However, the difference in the reactivity of the alginate extracts, *i.e.,* 0.33 and 0.34 mg/min for RSWE and BSWE, respectively, compared to 0.16 mg/min for commercial-grade alginate (*see* Table 2), could be an indicator that the isolated alginates were not pure. These residual impurities, including proteins, fatty acids, and other non-polysaccharide constituents, can influence the properties of the resulting bioplastics. For instance, they may reduce mechanical strength, alter thermal stability, and affect film-forming efficiency, potentially leading to decreased homogeneity or increased brittleness in the final films. The DTG curves for the films (Fig. 2f) indicate that the material synthesized from BSW closely resembles the bioplastic synthesized *via* a control experiment where a commercial-grade alginate was used (CEBP). This is evidenced by the similarity between the DTG curve of BSWBP and that of CEBP. The relative purity of the bioplastic films, estimated from the areas under the DTG curves, was *ca.* 87 % for BSWBP and 47 % for RSWBP. Furthermore, the thermal degradation characteristic parameters for BSWBP and CEBP presented in Table 2 are comparable. In contrast, the DTG curve and thermal degradation characteristic parameters of RSWBP exhibit a markedly different profile from that of CEBP. This divergence suggests that the proteins and other constituents detected in the original RSW sample adversely influenced the quality of the resulting film. A rough estimate of the relative purity of the synthesised bioplastics can be determined from the areas under the DTG curves, where it is clear that BSWBP had higher purity compared to RSWBP. This observation indicates that the bioplastic derived from BSW contained fewer impurities and a higher proportion of polysaccharides, resulting in a material more comparable in quality to the control alginate-based film. In contrast, the lower purity of RSWBP suggests the presence of residual proteins and other non-polysaccharide constituents, which likely compromised its structural and thermal properties [43,44].

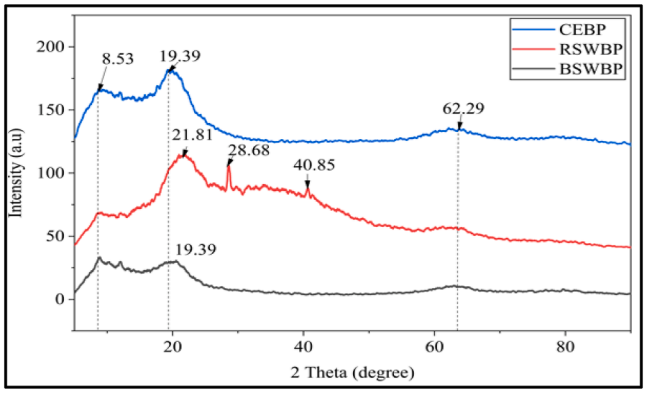


**Fig. 1.** XRD patterns of bioplastic films showing their structural characteristics.

FT-IR results for the seaweed samples (Fig. 2*g*) reveal the presence of polysaccharides, amino acids, aliphatic compounds, and inherent moisture as evidenced by broad peaks at 3300 $cm^{-1,}$ which are a result of O—H and N—H bond stretching. Because the cellulose and lignin in seaweed contain sulphates and phenols, peaks at 1200 $cm^{-1}$ and 650 $cm^{-1}$ are as a result of *S═O*, C—O, C—S, and *C═S* bond stretching. Strong absorption peaks at 1025 and 1030 $cm^{-1}$ indicate *S═O* stretching or C—O elongation, which suggests the presence of polysaccharides and starch. Absorption peaks observed around 1600 to 1800 $cm^{-1}$ indicate the presence of *C═O* and *N═O* stretching, suggesting the presence of esters and amides. The peaks ranging from 400 to 900 $cm^{-1}$ indicate the presence of C—S and *C═S* stretching within sulphates and disulphides. Following the extraction process, the FT-IR spectra (Fig. 2h) of the seaweed extracts (BSWE and RSWE) displayed characteristic peaks at 800, 1025, and 1030 $cm^{-1}$, confirming the presence of polysaccharides and starch. The overlaid spectrum of SA exhibited similar peaks, supporting the successful extraction of alginate. The characteristic SA peaks reported by Pereira *et al.* [45] and Rao *et al.* [46] were observed at *ca.* 3427, 2934, 1635, 1400, 1300, 1256, and 1079 $cm^{-1}$, corresponding to O—H stretching (3427 $cm^{-1}$), C—H stretching (2934 $cm^{-1}$), asymmetric and symmetric stretching of carboxylate groups (1635 and 1400 $cm^{-1}$), C—O—C glycosidic linkages (1300 and 1079 $cm^{-1}$), and C—O stretching of uronic acid units (1256 $cm^{-1}$). However, the spectra do not completely overlap, as the extracts exhibit additional peaks that are indicative of residual impurities. These peaks are likely associated with functional groups from proteins and other constituents

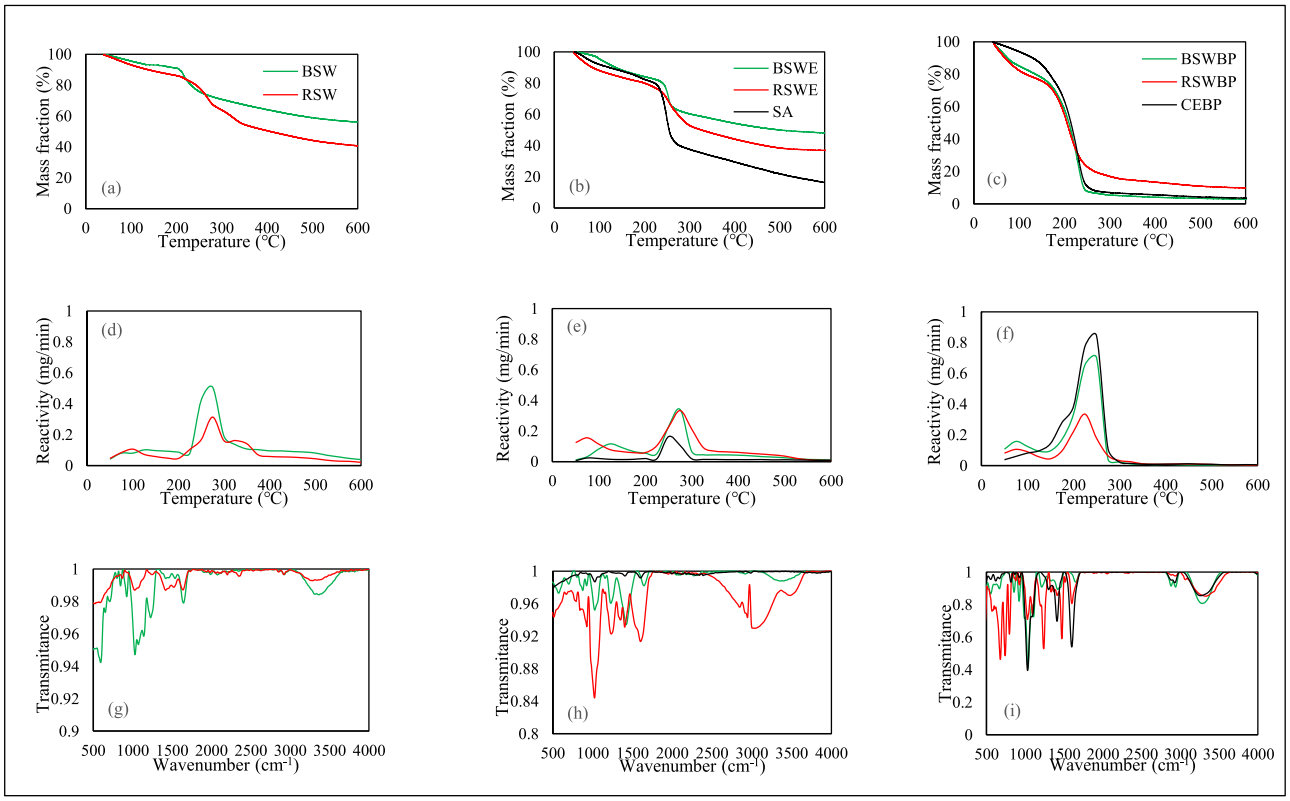


**Fig. 2.** TG, DTG, and FT-IR characterization of seaweed-derived bioplastics and their precursors.

**Table 2**
Thermal degradation characteristic parameters of seaweeds, extracts, and resultant bioplastics.

| Parameter | Sample code | | | | | | | |
|---|---|---|---|---|---|---|---|---|
| | BSW | RSW | BSWE | RSWE | SA | BSWBP | RSWBP | CEBP |
| $T_o$ (°C) | 225 | 200 | 225 | 200 | 225 | 150 | 150 | 150 |
| $T_p$ (°C) | 275 | 275 | 275 | 275 | 250 | 250 | 225 | 250 |
| $T_f$ (°C) | 350 | 400 | 325 | 350 | 325 | 275 | 325 | 275 |
| $R_p$ (mg/min) | 0.51 | 0.31 | 0.34 | 0.33 | 0.16 | 0.70 | 0.33 | 0.84 |

that were not fully eliminated during the extraction process. The FT-IR spectra (Fig. 2i) for the synthesised bioplastics show good correspondence with the control bioplastic, especially for the BSWBP. For the BSWBP spectrum, there are a few peaks that do not appear on the control spectrum, namely, the peak at 1220 $cm^{-1}$, which corresponds to C—O bond stretching most probably from phenolic O—H groups found in lignin. For the RSWBP spectrum, the presence of several additional peaks that do not conform to the control further supports the conclusion drawn from the DTG analysis, *i.e.,* the bioplastic synthesized exhibited lower relative purity. To improve extract purity and enhance bioplastic quality, additional purification steps could be considered. Methods such as repeated precipitation, dialysis, enzymatic treatment, or column-based separation may help remove residual proteins and other impurities, resulting in films with more uniform structure, better mechanical properties, and improved thermal performance. The prominent impurity peaks appear at 730, 795, 1500, and 1520 $cm^{-1}$, corresponding to N—H, C—S, and *C*═*C* vibrations typically associated with proteins, fatty acids, lignin, and sulphates.

### 3.4. Thermal degradation behaviour

TGA curves showing the mass-loss due to thermal degradation at different heating rates for the three bioplastic films are shown in Fig. 3. As can be seen, the temperature of maximum degradation rate increases with the increase of heating rate, *i.e.,* the peak shifts to the right along the horizontal axis. The resistance to heat and mass transfer inside the sample structure implies that degradation reactions do not have enough time to reach completion at lower temperatures. At higher heating rates, the biomass reaches a given temperature faster, requiring the degradation processes to occur at a higher temperature to achieve the same degree of mass loss, resulting in a shift of the peaks to the right. Two main reasons can be attributed to this phenomenon. Firstly, the temperature variation changes between the instrument furnace and the samples with the increasing heating rate. Secondly, thermal decomposition is a kinetic process that depends on both temperature and time [45,46]. The DSC curves in Fig. 3 show heat flow within the sample during the thermal degradation process. Endothermic peaks appear at a temperature range of ≈ 220 to 260 °C; also, the DTG curves reveal that there is a significant thermal degradation event that occurs at the same temperature range, as evidenced by the DTG peaks. At this temperature range, the main chain of the bioplastic films begins to break down into polymer fragments, then further produces small molecules that escape as volatile matter, resulting in a mass loss of the sample. At higher heating rates, *i.e.,* 15 and 20 °C/min, the endothermic peaks are more pronounced, which is consistent with the DTG curves, whereby it is clear that the reactivity of the bioplastic samples increases. The maximum degradation rate of the bioplastic films occurs at a temperature of 250 °C and a heating rate of 20 °C/min and is in the range 0.92 to 1.00 mg/min.

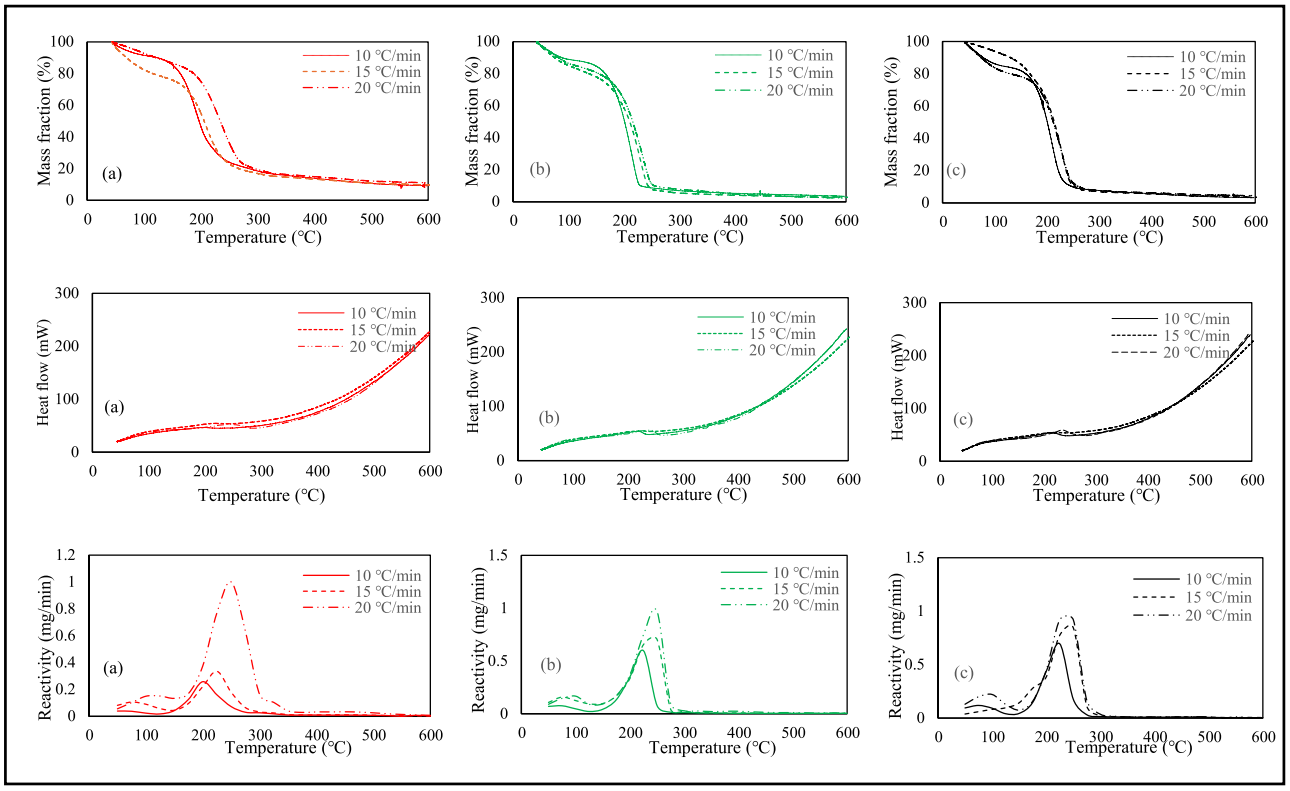


**Fig. 3.** Thermograms of RSWBP (a), BSWBP (b), and CEBP (c), each showing TG, DTG, and DSC results obtained at different heating rates.

In general, biomass pyrolysis reactivity increases with higher heating rates because thermal decomposition is a kinetic process that depends on both temperature and time. Also, at high heating rates, there are reduced heat and mass transfer limitations within the biomass particle, allowing for more efficient and rapid decomposition and higher rates of mass loss. Furthermore, when the heating rate is sufficiently low during pyrolysis, most of the individual constituents tend to decompose separately and give individual peaks on the DTG curve. However, at high heating rates, the constituents tend to decompose simultaneously; therefore, on the DTG curve, several adjacent peaks are united to form overlapped, broader, and higher peaks [47]. Approximate glass transition temperature ($T_g$) can be determined *via* DSC thermograms when the heat flow is reported per unit mass change. As it can be seen on Fig. 4, the $T_g$s of the bioplastic films were determined to be in the range 50 – 60 °C at a heating rate of 15 °C/min. This value is consistent with $T_g$ values that have been reported elsewhere [48]. It is worth noting that the DSC curves in Fig. 3 do not display clear $T_g$ peaks unless the axis scale is enlarged, as shown in Fig. 4. This behaviour is common in DSC analyses of bioplastics, as also reported by Zhang *et al.* [49], and is generally attributed to their high crystallinity and low amorphous content, which result in very weak or undetectable $T_g$ and cold crystallization peaks.

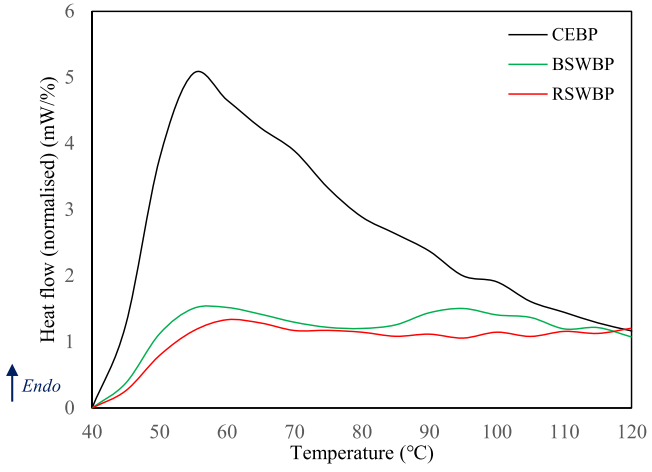


**Fig. 4.** DSC thermograms indicating the glass transition temperatures of the synthesized bioplastic films.

### 3.5. Degradation kinetics analysis

#### 3.5.1. Model-free methods

The variation of activation energies with conversion, as evaluated by the KAS and OFW methods, is given in Table 3. The two methods are reliable in the kinetic analysis of the thermal degradation of RSWBP, as evidenced by high $R^2$ values which are close to unity. In general, model-free methods are primarily used to determine the $E_a$ as a function of conversion without assuming a reaction model. However, these methods are not used to directly deduce other reaction parameters, such as the rate constant ($k$), because they depend not only on $E_a$ but also on the pre-exponential factor ($A$) and the reaction model function $f(X)$ in the Arrhenius expression [31,50]. The average activation energies of the three bioplastic samples, as determined by the KAS method, were 20.0, 43.8, and 44.7 kJ/mol for RSWBP, BSWBP, and CEBP, respectively. Using the OFW method, the corresponding values were evaluated at slightly higher values of 26.8, 49.5, and 50.4 kJ/mol. These results indicate that the thermal degradation behavior of BSWBP closely resembles that of CEBP, thereby reinforcing the earlier conclusions drawn from the TGA and FT-IR analyses. Generally, these results are in agreement with the works of Wahyuningtiyas *et al.* [51], who reported an $E_a$ of cassava starch bioplastic of 22 kJ/mol, and Oliver *et al.* [52], who reported an $E_a$ of 65 kJ/mol for thermoplastic starch made from potatoes.

The variation of activation energies around the mean is expressed in terms of the relative standard deviation (Table 3). In our previous work,

**Table 3**
Thermal degradation activation energies evaluated *via* the KAS and OFW methods.

| | KAS | | | | | | OFW | | | | | |
|---|---|---|---|---|---|---|---|---|---|---|---|---|
| | BSWBP | | RSWBP | | CEBP | | BSWBP | | RSWBP | | CEBP | |
| | $R^2$ | $E_a$ (kJ/mol) | $R^2$ | $E_a$ (kJ/mol) | $R^2$ | $E_a$ (kJ/mol) | $R^2$ | $E_a$ (kJ/mol) | $R^2$ | $E_a$ (kJ/mol) | $R^2$ | $E_a$ (kJ/mol) |
| Conversion | | | | | | | | | | | | |
| 0.1 | 0.78 | 37.0 | 0.98 | 18.7 | 0.78 | 37.1 | 0.84 | 42.9 | 0.99 | 25.3 | 0.84 | 43.0 |
| 0.2 | 0.81 | 39.4 | 0.98 | 19.2 | 0.79 | 39.3 | 0.86 | 45.2 | 0.99 | 25.8 | 0.84 | 45.1 |
| 0.3 | 0.83 | 41.3 | 0.98 | 19.4 | 0.79 | 41.1 | 0.87 | 47.0 | 0.99 | 26.2 | 0.85 | 46.9 |
| 0.4 | 0.85 | 43.2 | 0.97 | 19.7 | 0.81 | 43.3 | 0.89 | 48.9 | 0.99 | 26.4 | 0.85 | 49.0 |
| 0.5 | 0.87 | 44.9 | 0.97 | 19.8 | 0.82 | 45.3 | 0.90 | 50.5 | 0.99 | 26.6 | 0.86 | 51.0 |
| 0.6 | 0.88 | 46.4 | 0.97 | 20.1 | 0.84 | 47.8 | 0.91 | 52.1 | 0.99 | 26.9 | 0.88 | 53.4 |
| 0.7 | 0.89 | 47.7 | 0.97 | 20.2 | 0.82 | 49.5 | 0.92 | 53.3 | 0.99 | 27.1 | 0.86 | 55.0 |
| 0.8 | 0.89 | 48.1 | 0.98 | 20.8 | 0.87 | 49.9 | 0.92 | 53.7 | 0.99 | 27.8 | 0.90 | 55.5 |
| 0.9 | 0.87 | 46.2 | 0.98 | 22.2 | 0.88 | 49.1 | 0.90 | 52.0 | 0.99 | 29.2 | 0.91 | 54.8 |
| Average | - | 43.8 | - | 20.0 | - | 44.7 | - | 49.5 | - | 26.8 | - | 50.4 |
| SD | - | 3.9 | - | 1.0 | - | 4.8 | - | 3.8 | - | 1.1 | - | 4.7 |
| RSD ( %) | - | 8.8 | - | 5.1 | - | 10.6 | - | 7.6 | - | 4.3 | - | 9.2 |

a deviation of ± 5 % from the mean was considered negligible [31]. However, in the present study, the results from both methods are at the limit or exceed this threshold. This discrepancy can be attributed to the inherent assumptions of the methods, whereby a simplified reaction scheme is assumed, whereas in reality, bioplastic decomposition involves a complex, multi-step, and multi-component degradation pathway [31]. Additional sources of variation, such as experimental noise, baseline shifts, and heating rate sensitivity, may also contribute. Nevertheless, the observed deviations likely reflect the true multi-step nature of the bioplastic thermal degradation process.

### 3.5.2. *Model-fitting methods*

Fig. 5 presents the linear plots obtained using the Kissinger method, where the slopes were used to determine the pyrolysis activation energies from the experimental mass loss data. The results are presented in Table 4.

From Table 4, it can be seen that the results of the Kissinger model-fitting method are in agreement with the KAS and OFW methods. The Kissinger method often agrees with KAS and OFW when the decomposition is dominated by a single-step mechanism with little variation in $E_a$ across conversion, meaning the process behaves close to a first-order reaction without significant multi-step overlapping effects. However, in this case, the activation energies evaluated by the KAS and OFW methods show some significant variation as the conversion increases. This indicates that the Kissinger method fails to detect the inherent complexity of the degradation processes [53].

Prior to the application of the CR method, the most suitable models were searched *via* the master-plots method [54–56]. The experimental data were tested against several models, namely, 0th order (R1), contracting cylinder (R2), contracting sphere (R3), 1st order reaction (F1), one-dimensional diffusion (D1), two-dimensional diffusion (D2), and nucleation (N1, N2, and N3) models. The results of the master plots method are presented in Fig. 6. It can be seen that the experimental data do not fit perfectly into one kinetic model; however, most of the experimental points are close to 1st order reaction and nucleation models. As such, the CR model-fitting method will be applied for the nucleation models whose mathematical functions for *G(X)* are presented in the works of Ceylan [57]. The Johnson–Mehl–Avrami–Kolmogorov model, or simply the Avrami equation, was originally designed to describe phase transformations in materials. However, its nucleation-and-growth framework has since been widely applied to model diverse phenomena across the life, physical, and social sciences, even beyond strictly thermodynamic systems [58]. The activation energies evaluated *via* the CR method are presented in Table 5.

**Table 4**
Activation energies for thermal degradation determined using the Kissinger method.

| Sample | $R^2$ | $E_a$ (kJ/mol) |
|---|---|---|
| RSWBP | 1.00 | 20.2 |
| BSWBP | 0.87 | 46.2 |
| CEBP | 0.87 | 48.8 |

The four nucleation models fitted to the experimental data produced

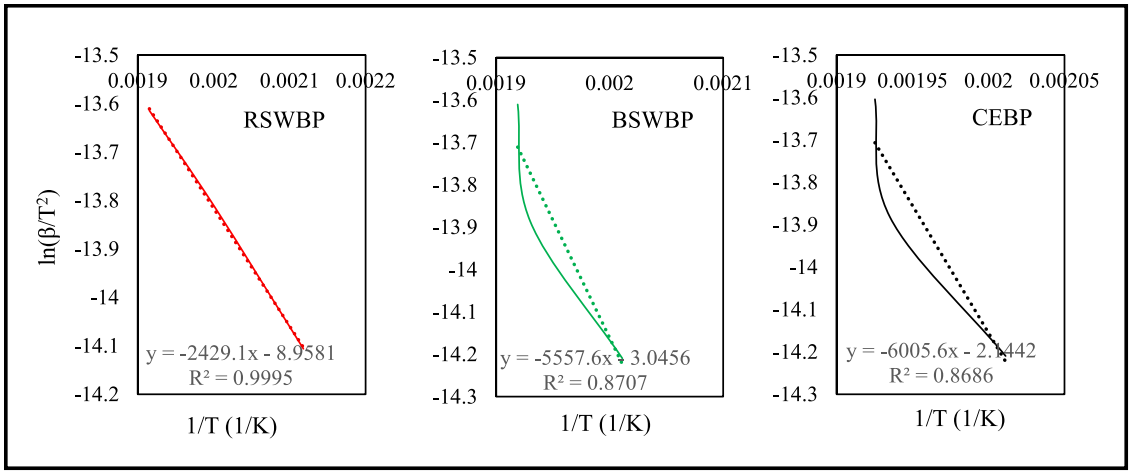


**Fig. 5.** Linear plots for the Kissinger method.

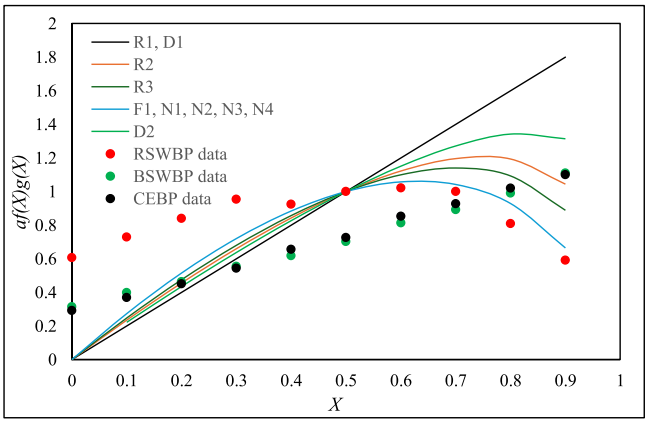


**Fig. 6.** Theoretical master plots for different kinetic models and experimental data.

**Table 5**
Activation energies for thermal degradation determined using the Coats–Redfern method.

| | 10 °C/min | | 15 °C/min | | 20 °C/min | | Average | |
|---|---|---|---|---|---|---|---|---|
| | $R^2$ | $E_a$ (kJ/mol) | $R^2$ | $E_a$ (kJ/mol) | $R^2$ | $E_a$ (kJ/mol) | $R^2$ | $E_a$ (kJ/mol) |
| *F1, N1* | | | | | | | | |
| RSWBP | 0.97 | 128.6 | 0.96 | 134.6 | 0.98 | 157.4 | 0.97 | 140.2 |
| BSWBP | 0.92 | 144.6 | 0.76 | 169.9 | 0.83 | 195.5 | 0.84 | 170.0 |
| CEBP | 0.95 | 130.4 | 0.92 | 76.6 | 0.93 | 129.0 | 0.93 | 112.0 |
| *N2* | | | | | | | | |
| RSWBP | 0.97 | 60.4 | 0.96 | 63.1 | 0.98 | 74.3 | 0.97 | 65.9 |
| BSWBP | 0.91 | 68.1 | 0.74 | 80.6 | 0.82 | 93.4 | 0.82 | 80.7 |
| CEBP | 0.94 | 61.0 | 0.91 | 60.0 | 0.92 | 60.2 | 0.92 | 60.4 |
| *N3* | | | | | | | | |
| RSWBP | 0.97 | 37.2 | 0.95 | 38.9 | 0.98 | 46.1 | 0.97 | 40.7 |
| BSWBP | 0.9 | 42.1 | 0.72 | 49.1 | 0.8 | 58.2 | 0.81 | 49.8 |
| CEBP | 0.93 | 37.5 | 0.9 | 36.7 | 0.91 | 36.7 | 0.91 | 37.0 |
| *N4* | | | | | | | | |
| RSWBP | 0.96 | 26.2 | 0.96 | 27.4 | 0.97 | 32.8 | 0.96 | 28.8 |
| BSWBP | 0.88 | 29.9 | 0.78 | 23.3 | 0.86 | 29.5 | 0.84 | 27.6 |
| CEBP | 0.92 | 26.4 | 0.88 | 25.7 | 0.9 | 25.7 | 0.9 | 25.9 |

high $R^2$ values (0.81 to 0.97) with apparent $E_a$ ranges of 28.8 to 140.2, 27.6 to 170.0, and 25.9 to 112.0 kJ/mol for RSWBP, BSWBP, and CEBP, respectively. When compared with the activation energies obtained through model-free methods, the decomposition kinetics of RSWBP most closely follow the N4 nucleation mechanism, whereas BSWBP and CEBP align with the N3 nucleation model. This difference can be attributed to structural and compositional variations among the samples. RSWBP likely possesses a more uniform polymer matrix and smaller particle size, which facilitates simultaneous multi-site nucleation consistent with the N4 model. In contrast, BSWBP and CEBP exhibit more heterogeneous structures, with varying crystallinity and thermal stability, favoring sequential nucleation and growth processes captured by the N3 model. These distinctions indicate that the intrinsic heterogeneity and complexity of the bioplastics strongly influence the preferential nucleation mechanism during thermal decomposition. Using the CR method, activation energies of 28.8, 49.8, and 37.0 kJ/mol were calculated for RSWBP, BSWBP, and CEBP, respectively, which are in good agreement with values from the Kissinger, KAS, and OFW methods. Interestingly, while the KAS and OFW model-free analyses suggest that decomposition does not proceed through a uniform set of first-order reactions because of the high variation of the activation energies around the mean and therefore cannot be captured by a single kinetic model, the Kissinger method, which is based on a single-step first-order assumption, still yields comparable activation energies at high $R^2$. By contrast, the CR method indicates that higher-order nucleation models, rather than the simple N1 model, which is in essence a first-order reaction kinetics model, dominate the decomposition process, as the N1 model produces anomalously high $E_a$ values. Furthermore, the suitability of the N3 and N4 models reflects the multi-step, overlapping nature of decomposition in these bioplastics. The higher-order nucleation models account for simultaneous or sequential growth of multiple degradation sites, which cannot be captured by the simpler N1 (first-order) model. This mechanistic perspective aligns with typical differences in particle morphology, polymer chain arrangement, and thermal heterogeneity, providing a more accurate description of the decomposition kinetics. This discrepancy can plausibly be attributed to the inherent complexity of bioplastic decomposition, which involves overlapping multi-step reactions and heterogeneous components. The simplifying assumptions of the Kissinger and the first-order CR models may artificially lower or raise $E_a$ estimates, whereas the higher-order nucleation fits better capture the multi-phase nature of the process. Essentially, the selection of the N3 and N4 nucleation models is consistent with the complex, multi-phase decomposition pathways of bioplastics, where structural heterogeneity dictates the predominance of specific nucleation mechanisms. As it has been mentioned before, experimental factors such as baseline shifts, heat transfer limitations, and compositional variability may also contribute to these variations.

## 4. Conclusion and future outlook

This study demonstrated the successful synthesis of bioplastic films from *S. oligocystum* and *E. spinosum* seaweeds and provided a significant analysis of their structural and thermal degradation behavior. Proximate and extraction analyses, together with FT-IR spectral features—including characteristic O–H, C–O, and glycosidic bond vibrations observed in the extracts and bioplastics—indicate that both seaweeds are rich in polysaccharides, mainly alginates and carrageenans, which serve as the primary film-forming agents. XRD and thermal analyses revealed that BSW-derived bioplastics exhibit higher amorphous content, superior thermal stability, and higher polysaccharide purity compared to RSW-based films, aligning closely with commercial alginate-based controls. Thermal degradation kinetics analyses using model-free (KAS, OFW) and model-fitting (Kissinger, Coats–Redfern) methods highlighted the complex, multi-step nature of thermal degradation, with higher-order nucleation mechanisms dominating for BSWBP and CEBP, whereas RSWBP displayed lower activation energies and structural heterogeneity. These findings establish *S. oligocystum* as a relatively more promising feedstock for producing bioplastics that are both thermally stable and biodegradable. Moving forward, optimizing extraction methods to enhance polysaccharide purity, reducing residual ash and protein content, and tailoring processing conditions will be critical for scaling up production. Future studies should also explore the mechanical, barrier, and biodegradability properties of these bioplastics under different natural environmental conditions (*e.g.,* soil, compost, and marine water), as well as their performance in composite formulations or as coatings, to further unlock the potential of seaweed-derived materials in sustainable packaging and circular economy applications. In addition, future investigations should incorporate quantitative determination of protein content, for example, through colorimetric assays such as the Bradford method, to complement proximate analysis and provide a deeper understanding of how residual proteins influence the structural integrity and thermal behavior of seaweed-based bioplastics. Further studies should also include complementary elemental characterization, such as CHNOS or related analyses, to validate the presence of S-bearing functional groups and strengthen the interpretation of FT-IR spectral features associated with sulfate or C–S vibrations.

## CRediT authorship contribution statement

**Alulutho Ngonyamana:** Methodology, Investigation, Formal

analysis. **Bothwell Nyoni:** Writing – original draft, Methodology, Investigation, Formal analysis, Data curation. **Jabulani I. Mnyango:** Writing – review & editing, Writing – original draft, Methodology, Formal analysis, Data curation. **Invine T. Kandirai:** Formal analysis. **Shanganyane P. Hlangothi:** Writing – review & editing, Supervision, Funding acquisition. **Sudhakar Muniyasamy:** Writing – review & editing, Funding acquisition, Conceptualization.

## Declaration of competing interest

The authors declare that they have no known competing financial interests or personal relationships that could have appeared to influence the work reported in this paper.

## Acknowledgements

We gratefully acknowledge the funding received from Nelson Mandela University and the National Research Foundation (NRF), as well as the CSIR Chemicals cluster parliament grant funding on bioplastic and bio-composite platform activities.

## Data availability

Data will be made available on request.

## References

[1] X. Zhao, Y. Wang, X. Chen, X. Yu, W. Li, S. Zhang, X. Meng, Z.-M. Zhao, T. Dong, A. Anderson, A. Aiyedun, Y. Li, E. Webb, Z. Wu, V. Kunc, A. Ragauskas, S. Ozcan, H. Zhu, Sustainable bioplastics derived from renewable natural resources for food packaging, Matter. 6 (2023) 97–127, https://doi.org/10.1016/j.matt.2022.11.006.

[2] F. Irfan, N. Tasnim, S.A. Razzak, S. Uddin, Advances in capturing carbon and producing bioplastics through the microalgal approach towards a sustainable future: a review, J. Clean. Prod 486 (2025) 144576, https://doi.org/10.1016/j.jclepro.2024.144576.

[3] K. Synani, K. Abeliotis, K. Velonia, A. Maragkaki, T. Manios, K. Lasaridi, Environmental impact and sustainability of bioplastic production from food waste, Sustain 16 (2024) 5529, https://doi.org/10.3390/su16135529.

[4] F. Haq, M. Kiran, I.A. Khan, S. Mehmood, T. Aziz, M. Haroon, Exploring the pathways to sustainability: a comprehensive review of biodegradable plastics in the circular economy, Mater. Today Sustain. 29 (2025) 101067, https://doi.org/10.1016/j.mtsust.2024.101067.

[5] S.I. Shofia, K. Jayakumar, A. Mukherjee, N. Chandrasekaran, Efficiency of brown seaweed (*Sargassum longifolium*) polysaccharides encapsulated in nanoemulsion and nanostructured lipid carrier against colon cancer cell lines HCT 116, RSC. Adv. 8 (2015) 15973–15984, https://doi.org/10.1039/C8RA02616E.

[6] L. Krishnan, N. Ravi, A.K. Mondal, F. Akter, M. Kumar, P. Ralph, U. Kuzhiumparambil, Seaweed-based polysaccharides – review of extraction, characterization, and bioplastic application, Green. Chem. 26 (2024) 5790–5823, https://doi.org/10.1039/D3GC04009G.

[7] C.M. Duarte, J. Wu, X. Xiao, A. Bruhn, D. Krause-Jensen, Can seaweed farming play a role in climate change mitigation and adaptation? Front. Marine Sci. 4 (2017) 100, https://doi.org/10.3389/fmars.2017.00100.

[8] I. Michalak, Chapter four - the application of seaweeds in environmental biotechnology, Adv. Bot Res 95 (2020) 85–111, https://doi.org/10.1016/bs.abr.2019.11.006.

[9] J. Cotas, L. Gomes, D. Pacheco, L. Pereira, Ecosystem services provided by seaweeds, Hydrobiol 2 (2023) 75–96, https://doi.org/10.3390/hydrobiology2010006.

[10] A. Chamas, H. Moon, J. Zheng, Y. Qiu, T. Tabassum, J.H. Jang, M. Abu-Omar, S. L. Scott, S. Suh, Degradation rates of plastics in the environment, ACS Sustain. Chem. Eng. 8 (2020) 3494–3511, https://doi.org/10.1021/acssuschemeng.9b06635.

[11] A.R. Bergeson, A.J. Silvera, H.S. Alper, Bottlenecks in biobased approaches to plastic degradation, Nature Comm 15 (2024) 4715, https://doi.org/10.1038/s41467-024-49146-8.

[12] M. Islam, T. Xayachak, N. Haque, D. Lau, M. Bhuiyan, B.K. Pramanik, Impact of bioplastics on environment from its production to end-of-life, Process Saf.. Environ. Prot. 188 (2024) 51–166, https://doi.org/10.1016/j.psep.2024.05.113.

[13] J. Stanley, D. Culliton, A.-J. Jovani-Sancho, A.C. Neves, The journey of plastics: historical development, environmental challenges, and the emergence of bioplastics for single-use products, Eng 6 (2025) 17, https://doi.org/10.3390/eng6010017.

[14] C. Lim, S. Yusoff, C.G. Ng, P.E. Lim, Y.C. Ching, Bioplastic made from seaweed polysaccharides with green production methods, J. Environ. Chem. Eng. 95 (2021) 105895, https://doi.org/10.1016/j.jece.2021.105895.

[15] M.M. El-Sheekh, E.A. Alwaleed, A. Ibrahim, H. Saber, Preparation and characterization of bioplastic film from the green seaweed Halimeda opuntia, Int. J. Biol. Macromol. 259 (2024) 129307, https://doi.org/10.1016/j.ijbiomac.2024.129307.

[16] G. Gunawan, H. Heryanto, D. Tahir, Keratin-based bioplastics extracted from chicken feathers: effect of chitosan concentration on the structural, chemical bonding, and mechanical properties of bioplastics, Int. J. Biol. Macromol. 265 (2024) 130722, https://doi.org/10.1016/j.ijbiomac.2024.130722.

[17] M. Amran, H. Ali, H. Issa, M. Sahini, S. Vuai, Assessment of baseline physicochemical qualities of carrageenan-based bioplastics from Kappaphycus alvarezii seaweed for their packaging applications, Carbohydr Polym. Technol. Appl. 10 (2025) 100790, https://doi.org/10.1016/j.carpta.2025.100790.

[18] Y. Chen, J.-Y. Han, G. Gao, J. Wang, W. Zhao, H. Yang, Y. Zhao, S. Wang, T. Zhang, Highly transparent, degradable, and robust bioplastic film for smart packaging, Polymer. (Guildf) 331 (2025) 128506, https://doi.org/10.1016/j.polymer.2025.128506.

[19] M.R. Ullah, M.A. Haque, M.M. Hasan, M.A. Islam, A. Bhadra, The influences of different drying procedures on the nutritional contents and antioxidant activities of brown seaweed, *sargassum oligocystum* mont. (Sargassaceae), Appl. Food Res. 5 (2025) 101055, https://doi.org/10.1016/j.afres.2025.101055.

[20] M.A.A. Khan, M.M. Hasan, M.K. Hossain, D. Adhikery, M. Hakim, L.C. Mohanta, A. S.M. Sharif, A.K. Sarker, Extraction and characteristic properties analyses of sodium alginate derived from the *Sargassum oligocystum* brown seaweed alga of the Bay of Bengal, Next Mater. 6 (2025) 100417, https://doi.org/10.1016/j.nxmate.2024.100417.

[21] G.-T. Jeong, Hydrothermal hydrolysis of macroalgae eucheuma spinosum by cationic resin catalyst for sugar recovery, Biomass Bioenergy 194 (2025) 107695, https://doi.org/10.1016/j.biombioe.2025.107695.

[22] M.S.F. Nurshahida, Z. Nazikussabah, S. Subramaniam, W.I.W. Faizal, M.A.N. Aini, IOP Conf. Ser.: Mater. Sci. Eng. 991 (2020) 012048, https://doi.org/10.1088/1757-899X/991/1/012048.

[23] Y. Hu, S. Wang, Q. Wang, Z. He, X. Lin, S. Xu, H. Ji, Y. Li, Effect of different pretreatments on the thermal degradation of seaweed biomass, Proc. Combust. Inst. 36 (2017) 2271–2281, https://doi.org/10.1016/j.proci.2016.08.086.

[24] R.L. Doval, K. Timmermans, R.P. de Vries, Marine fungal enzymes as potential degraders of the diverse seaweed cell-walls, Biotechnol. Adv. 83 (2025) 108653, https://doi.org/10.1016/j.biotechadv.2025.108653.

[25] E. Martínez-Martínez, A.H. Slocum, M.L. Ceballos, P. Aponte, A.G. Bisonó-León, Beyond the bloom: invasive seaweed *sargassum spp.* As a catalyst for sustainable agriculture and blue economy—A multifaceted approach to biodegradable films, biostimulants, and carbon mitigation, Sust 17 (2025) 3498, https://doi.org/10.3390/su17083498.

[26] H.L. Ornaghi, M. Faccio, M.R.F. Soares, Thermal degradation kinetics of natural fibers: determination of the kinetic triplet and lifetime prediction, Polysaccharides 5 (2024) 169–183, https://doi.org/10.3390/polysaccharides5030013.

[27] I. Lalaymia, A. Belaadi, D. Ghernaout, Studying gaussian deconvolution and multicomponent kinetics models in *Agave* cellulosic fibers pyrolysis: application in sustainable bioenergy for cleaner production, Biomass Bioenergy 192 (2025) 107488, https://doi.org/10.1016/j.biombioe.2024.107488.

[28] H. Bojorges, A. López-Rubio, A. Martínez-Abad, M.José Fabra, Overview of alginate extraction processes: impact on alginate molecular structure and techno-functional properties, Trends. Food Sci. Technol. 140 (2023) 104142, https://doi.org/10.1016/j.tifs.2023.104142.

[29] ASTM, E871-82(2019), Standard test method for moisture analysis of particulate wood fuels, [online] available at https://doi.org/10.1520/E0871-82R19, (accessed June 2024).

[30] ASTM, E872-82(2019), Standard test method for volatile matter in the analysis of particulate wood fuels, [online] available at https://doi.org/10.1520/E0872-82R19, (accessed June 2024).

[31] Y.-S. Cho, M.-J. Shim, S.-W. Kim, Thermal degradation kinetics of PE by the Kissinger equation, Mat. Chem. Phys. 52 (1998) 94–97, https://doi.org/10.1016/S0254-0584(98)80013-8.

[32] B. Nyoni, S. Duma, S.V. Shabangu, S.P. Hlangothi, Comparison of the slow pyrolysis behaviour and kinetics of coal, wood and algae at high heating rates, Nat. Resour. Res. 29 (2020) 3943–3955, https://doi.org/10.1007/s11053-020-09687-3.

[33] X. Zhang, Applications of kinetic methods in thermal analysis: a review, Eng. Sci. 14 (2021) 1–13, https://doi.org/10.30919/es8d1132.

[34] G. Adhityatama, F. Hanif, R. Cahyono, M. Hidayat, T. Akiyama, A comparative study on pyrolysis characteristic Indonesia biomassa and low-grade coal, IOP Conf. Ser.: Earth Environ. Sci. 65 (2017) 1–7, https://doi.org/10.1088/1755-1315/65/1/012001.

[35] J.E. White, W.J. Catallo, B.L. Legendre, Biomass pyrolysis kinetics: a comparative critical review with relevant agricultural residue case studies, J. Anal. Appl. Pyrolysis 91 (2011) 1–33, https://doi.org/10.1016/j.jaap.2011.01.004.

[36] E. Tarani, K. Chrissafis, Isoconversional methods: a powerful tool for kinetic analysis and the identification of experimental data quality, Thermochim. Acta 733 (2024) 1–14, https://doi.org/10.1016/j.tca.2024.179690.

[37] K.N. Chowdhury, M.K. Ahmed, K.T. Akhter, M.J. Alam, S. Rani, M.I. Khan, Proximate composition of some selected seaweeds from coastal areas of Cox's Bazar and the St. Martin's Island, Bangladesh, The Dhaka Univ. J. Earth Environ. Sci. (2022), https://doi.org/10.3329/dujees.v10i3.59077, 133–122.

[38] A.D. Premarathna, R. Tuvikene, P.H.P. Fernando, R. Adhikari, M.C.N. Perera, T. H. Ranahewa, M.M. Howlader, P. Wangchuk, A.P. Jayasooriya, R.P.V.J. Rajapakse, Comparative analysis of proximate compositions, mineral and functional chemical groups of 15 different seaweed species, Sci. Report. 12 (2022) 1–13, https://doi.org/10.1038/s41598-022-23609-8.

[39] N. Rajendran, S. Puppala, M.S. Raj, B.R. Angeeleena, C. Rajam, Seaweeds can be a new source for bioplastics, J. Pharma. Res. 5 (2012) 1476–1479.
[40] M.C. Zambrano, J.J. Pawlak, R.A. Venditti, Effects of chemical and morphological structure on biodegradability of fibers, fabrics, and other polymeric materials, BioRes 15 (2020) 9786–9833, https://doi.org/10.15376/biores.15.4.Zambrano.
[41] H.F. Sangian, E. MAneking, S.H.J. Tongkukut, H.I.R. Mosey, V. Suoth, H. Kolibu, A. Tanauma, G. Pasau, A. As'ari, V.A.J. Masinambow, B.A. Sadjab, M.M. Sangi, S. B. Rondonuwu, Study of SEM, XRD, TGA, and DSC of cassava bioplastics catalysed by ethanol, IOP Conf. Ser.: Mater. Sci. Eng. 1115 (2021) 012052, https://doi.org/10.1088/1757-899X/1115/1/012052.
[42] N. Khan, K. Sudhakar, R. Mamat, Thermogravimetric analysis of marine macroalgae waste biomass as bio-renewable fuel, J. Chem. (2022) 6417326, https://doi.org/10.1155/2022/6417326.
[43] A. Nesic, S. Meseldzija, S. Benavides, F.A. Figueroa, G. Cabrera-Barjas, Seaweed as a valuable and sustainable resource for food packaging materials, Foods. 13 (2024) 3212, https://doi.org/10.3390/foods13193212.
[44] E. Moore, D. Colbert, Ocean plastics: extraction, characterization and utilization of macroalgae biopolymers for packaging applications, Sust 16 (2024) 7175, https://doi.org/10.3390/su16167175.
[45] L. Pereira, Macroalgae, Encyclopedia (Basel,. 2021) 1 (2021) 177–188, https://doi.org/10.3390/encyclopedia1010017.
[46] K.M. Rao, K.S.V.K. Rao, P. Sudhakar, K.C. Rao, M.C.S. Subha, Synthesis and characterization of biodegradable poly (vinyl caprolactam) grafted on to sodium alginate and its microgels for controlled release studies of an anticancer drug, J. Appl. Pharma. Sci. 3 (2013) 61–69, https://doi.org/10.7324/JAPS.2013.3609.
[47] H. Haykiri-Acma, S. Yaman, S. Kucukbayrak, Effect of heating rate on the pyrolysis yields of rapeseed, Renew. Energy 31 (2006) 803–810, https://doi.org/10.1016/j.renene.2005.03.013.
[48] J. O'Laughlin, D. Doherty, B. Herward, C. McGleenan, M. Mahmud, P. Bhagabati, A.N. Boland, B. Freeland, K.D. Rochfort, S.M. Kelleher, S. Fahy, J. Gaughran, The potential of bio-based polylactic acid (PLA) as an alternative in reusable food containers: a review, Sustainability. 15 (2023) 15312, https://doi.org/10.3390/su152115312.
[49] M. Zhang, Y. Zhang, C. Li, N. Jing, S. Shao, F. Wang, H. Mei, K.M. Rogers, X. Kong, Y. Yuan, Identification of biodegradable plastics using differential scanning calorimetry and carbon composition with chemometrics, J. Hazardous Mater. Adv. 10 (2023) 100260, https://doi.org/10.1016/j.hazadv.2023.100260.
[50] B. Nyoni, S. Duma, L. Bolo, S. Shabangu, S. Hlangothi, Co-pyrolysis of South African bituminous coal and *scenedesmus* microalgae: kinetics and synergistic effects study, Int. J. Coal Sci. Technol. 7 (2020) 807–816, https://doi.org/10.1007/s40789-020-00310-7.
[51] N.E. Wahyuningtiyas, H. Suryanto, E. Rudiyanto, Thermogravimetric and kinetic analysis of cassava starch based bioplastic, J. Mech. Eng. Sci. Technol. 1 (2017) 1–16, https://doi.org/10.17977/um016v1i22017p069.
[52] I. Oliver, J.A. Conesa, A. Fullana, Thermal decomposition of bio-based plastic materials, Molecules. 29 (2024) 3195, https://doi.org/10.3390/molecules29133195.
[53] S. Vyazovkin, Kissinger method in kinetics of materials: things to beware and be aware of, Molecules. 25 (2020) 2813, https://doi.org/10.3390/molecules25122813.
[54] J.M. Criado, J. Malek, A. Ortega, Application of the master plots in kinetic analysis of non-isothermal data, Thermochim. Acta 147 (1989) 377–385, https://doi.org/10.1016/0040-6031(89)85192-5.
[55] D.I. Islan, P. Parthasarathy, J.L. Goldfarb, S. Ceylan, Pyrolysis reaction models of waste tires: application of Master-Plots method for energy conversion via devolatilization, Waste Manage., 68 (2017) 405–411, https://doi.org/10.1016/j.wasman.2017.06.006.
[56] L.M.R. Millán, F.E.S. Varga, A. Nzihou, Kinetic analysis of tropical lignocellulosic agrowaste pyrolysis, Bioenerg. Eng. 10 (2017) 832–845, https://doi.org/10.1007/s12155-017-9844-5.
[57] S. Ceylan, Kinetic analysis on the non-isothermal degradation of plum stone waste by thermogravimetric analysis and integral Master-Plots method, waste manage, Res., 33 (2015) 345–352, https://doi.org/10.1177/0734242×15574590.
[58] K. Shirzad, C. Viney, A critical review on applications of the Avrami equation beyond materials science, Interface 20 (2023) 20230242, https://doi.org/10.1098/rsif.2023.0242.